Supporting Information

Unveiling the Optical Parameters of Vanadium Dioxide in the Phase Transition Region: A Hybrid Modeling Approach

Mehmet Cihan Cakir, Hasan Kocer*, Yilmaz Durna, Deniz Umut Yildirim, Amir Ghobadi, Hodjat Hajian, Koray Aydin, Hamza Kurt, Necdet Saglam, Ekmel Ozbay**

1. Measured and simulated spectral reflectivity maps

We present the experimental ($R_{FTIR}(T, \lambda)$) and simulated ($R_{TMM}(T, \lambda)$) spectral reflectivity maps for "sample A" during heating (Figure S1(a) and S1(b)) and cooling (Figure S1(c) and S1(d)). From these 2D visualizations, it is easily seen that in each of the heating and cooling processes, $R_{FTIR}(T, \lambda)$ and $R_{TMM}(T, \lambda)$ are well compatible with each other at the specified temperature and wavelength ranges.

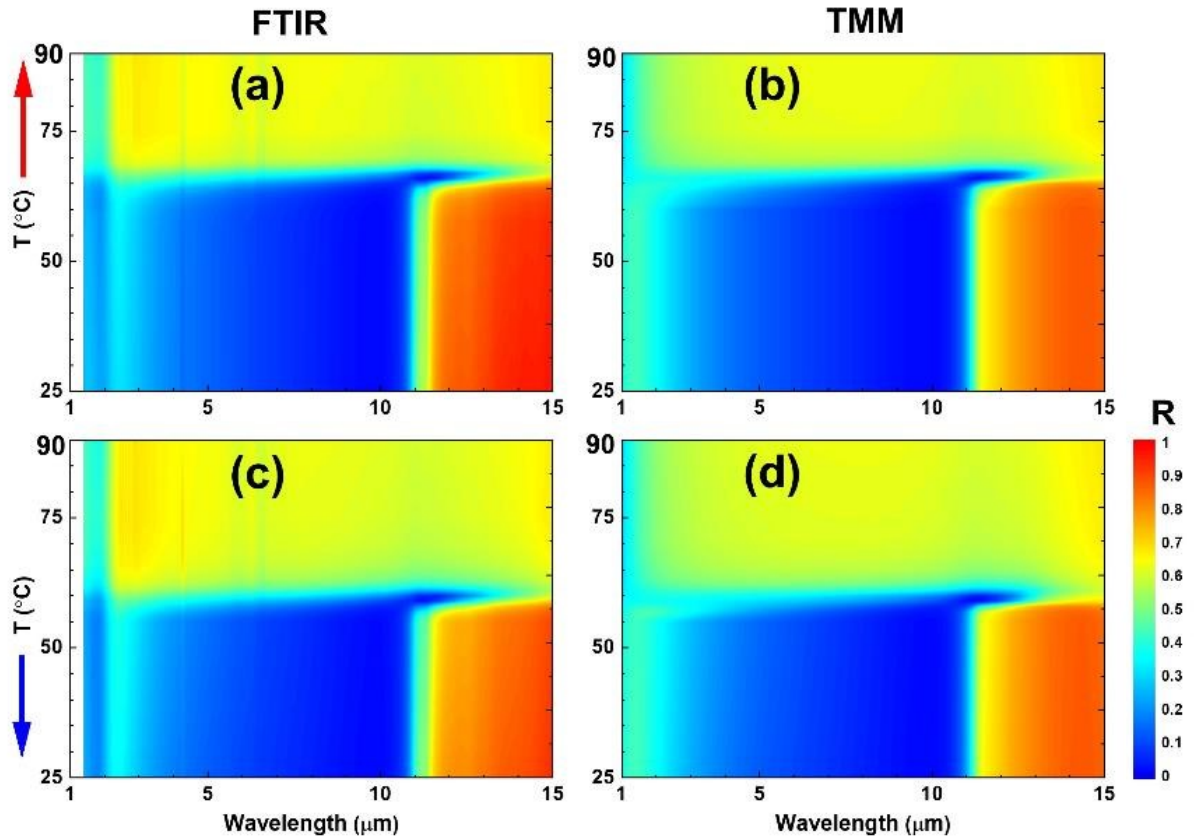

Figure S1. "Sample A" is illuminated from the VO_2 side. Spectral reflectivity (R) maps during heating: (a) Measured (FTIR) and (b) simulated (TMM). Spectral reflectivity maps during cooling: (c) FTIR and (d) TMM. The color bar applies to all.

2. Maps of the extracted infrared spectral optical parameters of VO_2

In order to better observe the variations with respect to temperature and the spectrum, the extracted spectral optical parameters of VO_2 in "sample A" are pictured as color maps in Figures S2 and S3 pursuant to the rising and descending temperature conditions. Accordingly, Figure S2(a) and S2(b) are respectively the real (n) and imaginary (K) parts of the spectral refractive indices of VO_2 in "sample A" as T increases. Figure S2(c) and S2(d) are the same parameters when the temperature is falling. In Figure S2(a) and S2(c), it is clearly seen under which temperature and wavelength conditions that the contour line of n = 1, which is of special importance due to its proximity to vacuum or air, is obtained.

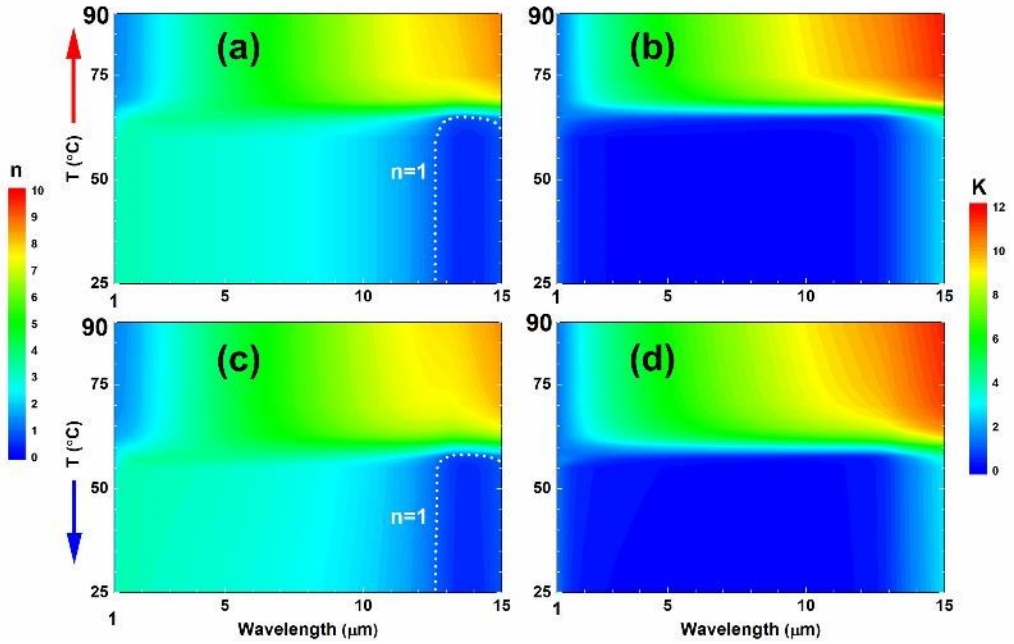

Figure S2. Maps of extracted infrared spectral refractive indices of VO_2 in "sample A" during heating: (a) Real (n) and (b) imaginary (K) parts. Maps of extracted infrared spectral refractive indices of VO_2 in "sample A" during cooling: (c) Real (n) and (d) imaginary (K) parts. The left color bar applies to (a) and (c). The right color bar applies to (b) and (d). The dotted white curves in (a) and (c) indicate the region in which the real part of the refractive index is one.

Similarly, the real (real ε_r) and the imaginary (imag. ε_r) parts of the spectral relative dielectric permittivities of VO_2 in "sample A" are indicated under heating (Figures S3(a) and S3(b)) and cooling (Figure S3(c) and S3(d)) cycles. Here, as another special case, the condition of real ε_r=0 (epsilon-near-zero, ENZ) appears in Figure S3(a) and S3(c) separately for heating and cooling

conditions. The ENZ region signifies a sudden change in the optical properties of the VO_2, as the crystal structure alters from the insulating phase to the metallic phase.[S1]

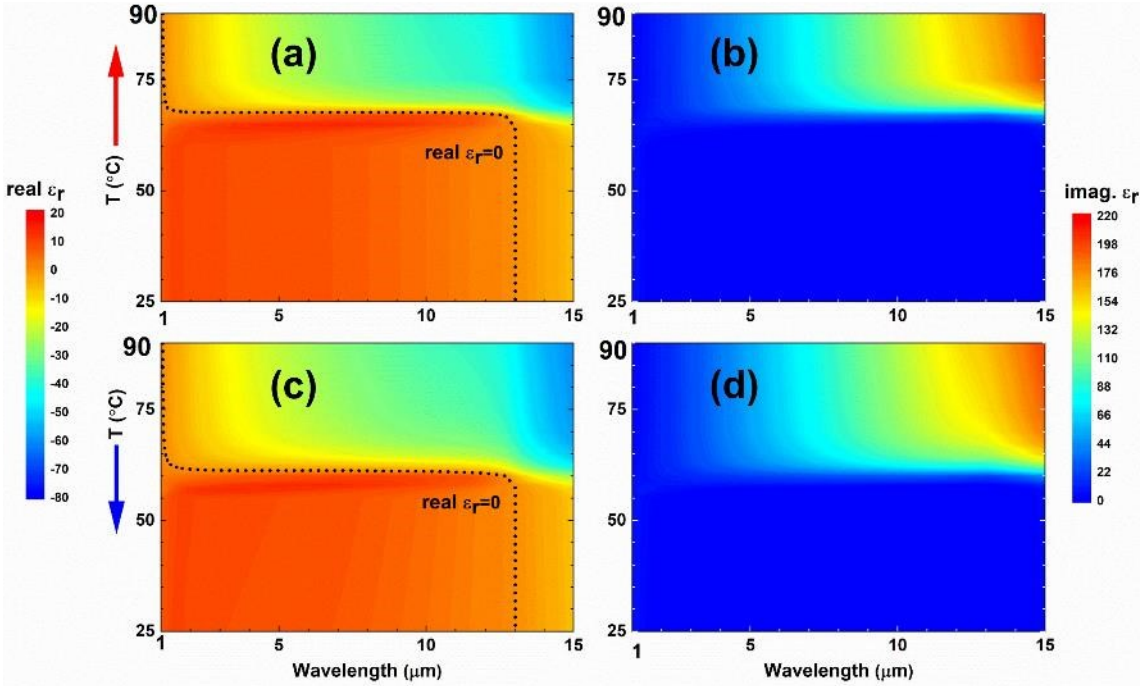

Figure S3. Maps of extracted infrared relative dielectric permittivities of VO_2 in "sample A" during heating: (a) Real (real ε_r) and (b) imaginary (imag. ε_r) parts. Maps of extracted infrared relative dielectric permittivities of VO_2 in "sample A" during cooling: (c) Real (real ε_r) and (d) imaginary (imag. ε_r) parts. The left color bar applies to (a) and (c). The right color bar applies to (b) and (d). The dotted black curves in (a) and (c) indicate the region in which the real part of the relative dielectric permittivity is zero (i.e. epsilon-near-zero, ENZ).

3. Additional hysteretic behaviors

Additional hysteretic behaviors are shown in Figure S4 for optical parameters at wavelengths λ=10 μm and 11.3 μm. Comparing the red and the blue colored data in terms of the hysteresis, we observe that the separation of the ENZ beginnings (Figure S4(a) and S4(c)) and the maximum widths across the linear regions (Figure S4(b) and S4(d)) in imag. ε_r are all the same values (i.e. ~7°C).

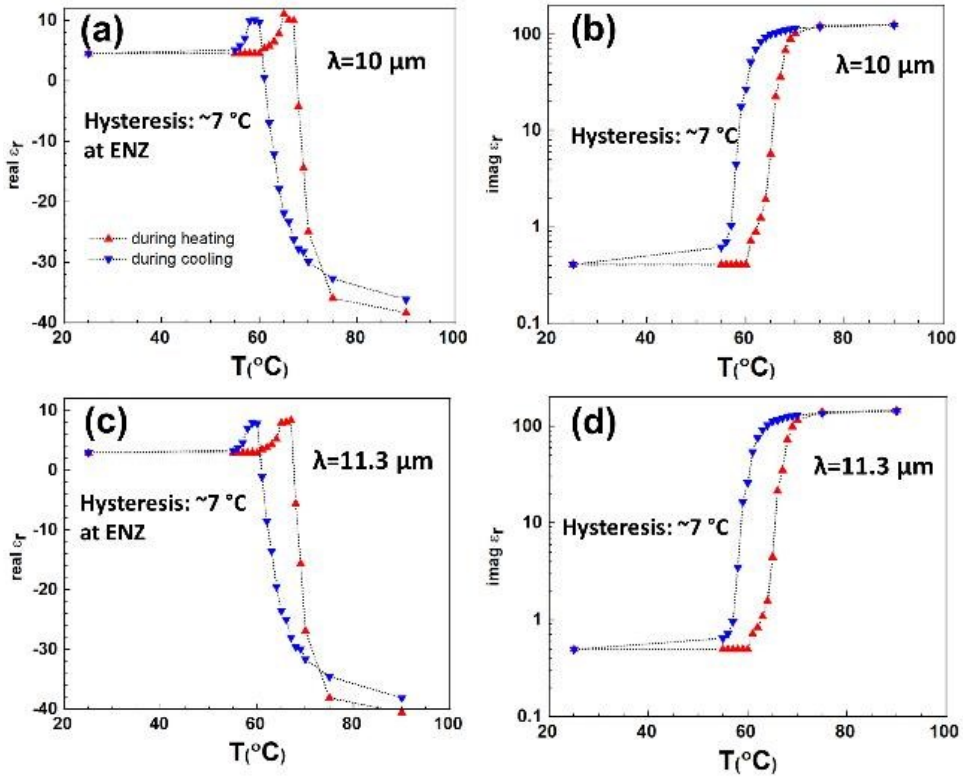

Figure S4. "Sample A" is illuminated from the VO_2 side. As the applied temperature to "sample A" increases and decreases, hysteretic behaviors observed in (a) real ε_r at λ=10 μm, (b) imag. ε_r at λ=10 μm, (c) real ε_r at λ=11.3 μm, (d) imag. ε_r at λ=11.3 μm.

4. Ellipsometer spectral data for SiO_2

Figure S5 depicts the measured ellipsometer (IR-VASE Mark II from J. A. Woollam Co. Inc.) spectral data for the real part of the refractive index (n) for SiO_2, which is utilized in this study. The imaginary part of the refractive index (K) for SiO_2 in this spectrum is found to be zero.

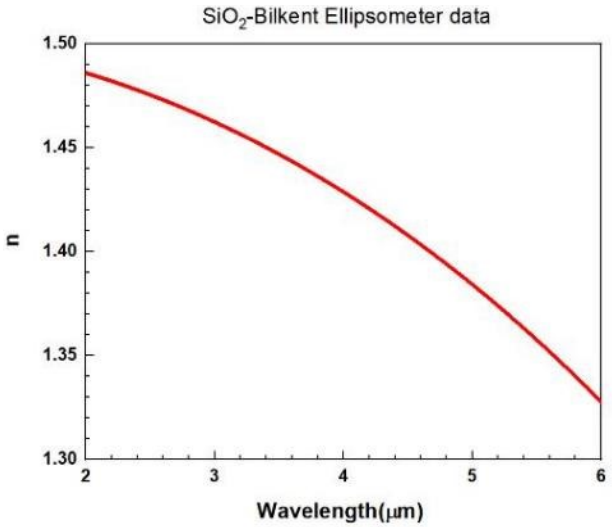

Figure S5. Measured ellipsometer spectral data for the real part of the refractive index (n) for SiO_2.

5. Numerical simulations to enlighten the physics behind the operating mechanism of the tunable device

For “sample C”, we obtained broadband and tunable reflection at SWIR and MWIR wavelengths through the experiments and simulations, which were given in the main text. Here, we perform finite-difference time-domain (FDTD) simulations with a commercial software from Lumerical Solutions[S2] in order to enlighten the physics behind this particular operating mechanism of the "sample C". In the FDTD simulations, we select λ=4 μm representing the wavelengths with the highest reflection contrast, and then send this wavelength in TM polarized plane wave at normal incidence. PML (perfectly matched layers) boundary conditions along the propagation axis and periodic boundary conditions along the axes that are perpendicular to the propagation are employed. The optical material parameters of the layers within the “sample C” were already mentioned in the main text. Then, electric field ($E(z, T)$), electric field intensity ($|E(z, T)|^2$), and absorbed power density (($P_{abs}(z, T)$) at λ=4 μm are determined in frequency domain and power monitors depending on the position (z) and the temperature (T). The absorbed power density is the divergence of the Poynting vector and can be calculated by[S3,S4]

$$P_{abs}(z,T) = \frac{\pi c}{\lambda}\varepsilon_0 \left[imag.\varepsilon_r(z,T)\right]\left|E(z,T)\right|^2 \quad \text{(S1)}$$

where c is the speed of the light in vacuum, ε_0 is the free space permittivity, imag. $\varepsilon_r(z, T)$ is the imaginary part of the relative dielectric permittivity, which varies with the space and the temperature. Figure S6 shows the resulting absorbed power density (Figure S6(a)), electric field intensity (Figure S6(b)), and optical parameters of the layers (Figures S6(c)-S6(f)) depending on the temperature and the location. When we look at the absorbed power density plots (Fig. S6(a)), we note that dominant absorption takes places inside the 90 nm-thick VO_2 layer at T=90°C (m-VO_2) although the electric field intensity of the insulating VO_2 at T=25°C (i-VO_2) is much higher than the m-VO_2 case (Fig. S6(b)). This situation can be easily explained with the aid of the plots in Figure S6(f) that the imag. ε_r(z=m-VO_2, T=90 °C) is approximately 40 times higher than the imag. ε_r(z=i-VO_2, T=25°C). In addition, there is also absorption occurring

inside the bottom Au-reflective layer, but this absorption is significantly lower than that of the top VO_2 layer due to the lesser field penetration into the optically thick Au layer.

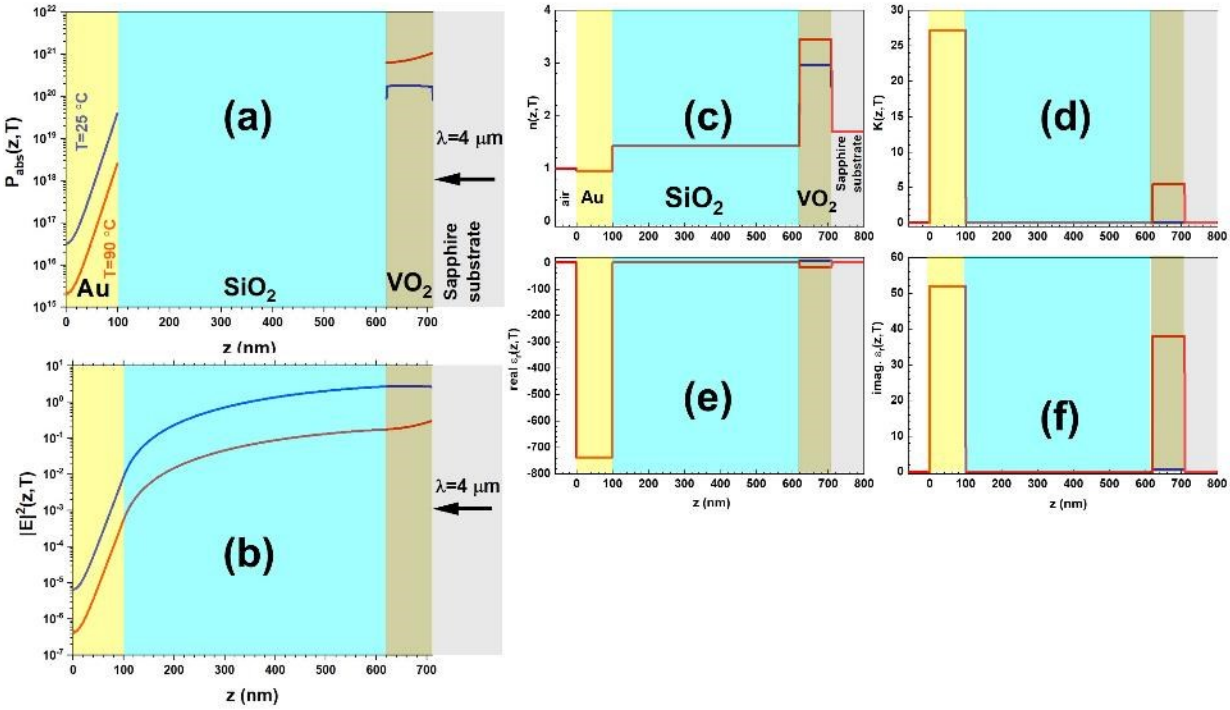

Figure S6. (a) Simulated (a) absorbed power density ($P_{abs}(z, T)$), (b) electric field intensity ($|E|^2(z, T)$), (c) real part of the refractive indices (n), (d) imaginary part of the refractive indices (K), (e) real part of the relative dielectric permittivities (real ε_r), and (f) imaginary part of the relative dielectric permittivities (imag. ε_r) along the structure at λ = 4 μm. Note that blue curves represent the values at T=25°C whereas red curves are the ones at T=90°C.

As computed hereinabove at λ = 4 μm, Figure S7 points out the spatial electric fields at T=25°C and T=90°C in different layers. In other words, the behaviors of $E(z, T)$ that cause the experimental and simulated reflection contrast (Figure 7S(a)) at λ = 4 μm for the "sample C" (inset in Figure-7S(a)) are displayed throughout the "sample C" including the sapphire substrate (Figure 7S(b)), the "sample C" excluding the substrate (Figure 7S(c)), and the gold bottom layer (Figure 7S(d)). In order to better visualize the electric fields along these layers at T=25°C and T=90°C, the $E(z, T)$ in the moving forms at these conditions are given in another supporting information (PPT).

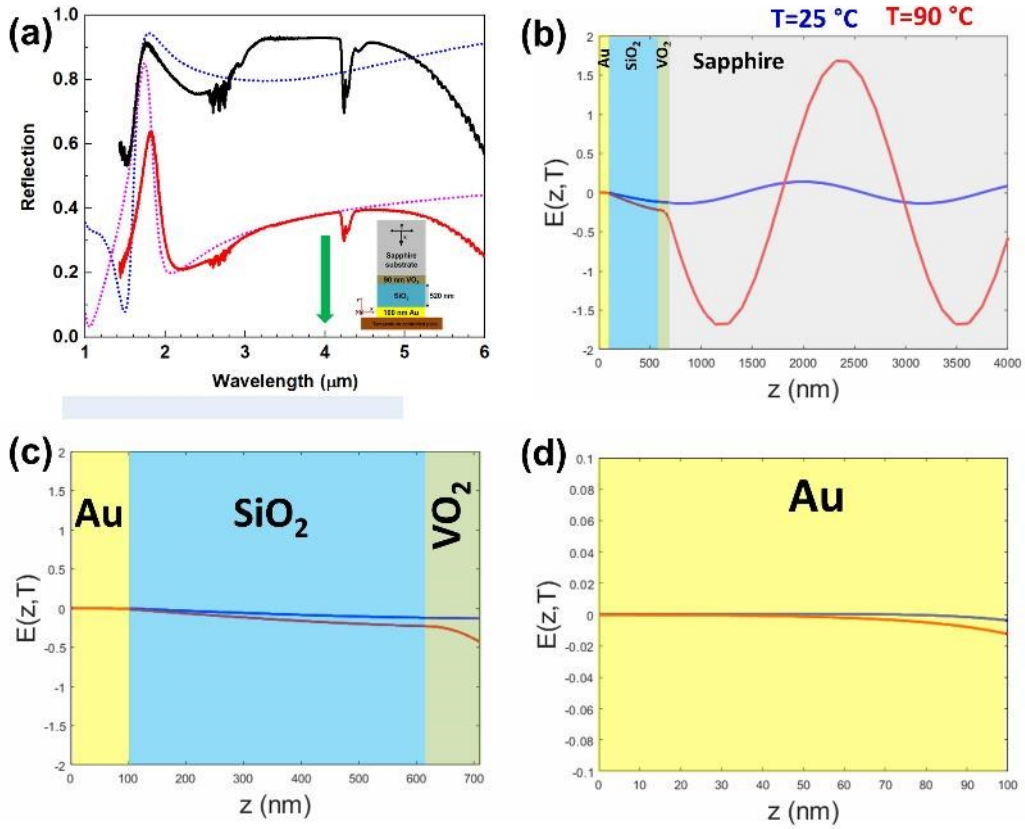

Figure S7. (a) TMM and FTIR reflection spectra of the structure shown in inset ("sample C") at T=25°C and T=90°C. Solid red (T=90°C) and black (T=25°C) curves represent FTIR power reflections whereas dotted pink (T=90°C) and blue (T=25°C) curves represent TMM power reflections. Animated electric fields ($E(z, T)$) at λ = 4 μm along (b) the structure extending the sapphire substrate, (c) the structure and (d) bottom gold layer. In (b) to (d), the blue curves are the field values at T=25°C, whereas red curves are the ones at T=90°C.

Under the conditions described in Figure S8, additional movies for the electric fields in the *x-z* plane under λ = 4 μm are provided in the supporting information (PPT) as well.

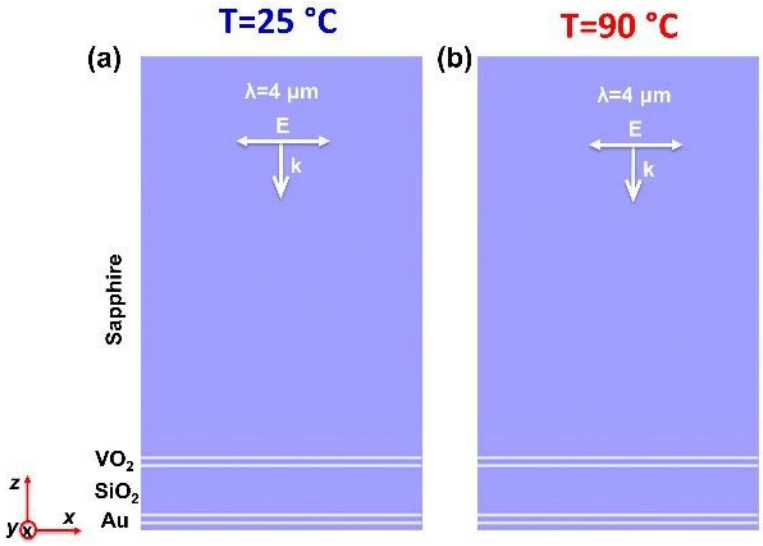

Figure S8. The movies for the electric fields in the *x-z* plane under λ = 4 μm at (b) T=25°C and (b) T=90°C.

REFERENCES

[S1] Y. Kim, P. C. Wu, R. Sokhoyan, K. Mauser, R. Glaudell, G. K. Shirmanesh and H. A. Atwater, *Nano Lett.*, 2019, **19**, 3961-3968.

[S2] Lumerical Home Page, https://www.lumerical.com/products/fdtd/.

[S3] K. Aydin, V. E. Ferry, R. M. Briggs and H. A. Atwater, *Nat. Commun.,* 2011, **2**, 517.

[S4] H. Kocer, S. Butun, E. Palacios, Z. Liu, S. Tongay, D. Fu, K. Wang, J. Wu and K. Aydin, *Sci. Rep*., 2015, **5**, 13384.